Eur. J. Mech. B - Fluids 20 (2001) 603–626

S0997-7546(01)01135-9/FLA

Vortex dynamics over a dihedral plane in a transitional slightly compressible flow: a computational study

E. Creusé [a,b], Iraj Mortazavi [a*]

[a] *Mathématiques Appliquées de Bordeaux, Université Bordeaux 1, 33405 Talence, France*
[b] *MACS, Université Valenciennes, le Mont Houy, 59313 Valenciennes cedex 9, France*

(Received 10 October 2000; revised 29 January 2001; accepted 21 February 2001)

Abstract – In this paper, three different vortex diagnostic methods are compared to obtain a better understanding of boundary layer influence on the transport of vortical structures involving a complete analysis of vorticity, the Vorticity Threshold Criterion (VTC), and the Weiss Criterion (WC). These three techniques are basically confronted to find a suitable understanding of all flow characteristics (the swirling dynamics produced downstream of the discontinuity point of the dihedral) for a range of laminar to transitional Reynolds numbers. The computations on this dihedral plane are made using a 2D DNS method. The Weiss criterion, coming from the analysis of the incompressible Euler equations is validated and applied to low speed compressible flows ($M = 0.2$). A detailed analysis of the swirling procedure is performed for Reynolds numbers 242, 400 (laminar), 565 and 800 (transitional). Finally, different averaged or instantaneous, local or global quantities are used to analyse and characterize Concentrated Structures as a function of the Reynolds number evolution. © 2001 Éditions scientifiques et médicales Elsevier SAS

Nomenclature

L	total length of the simulation domain
h	height of the domain
l	distance AB
x_0	distance of A from the attack point
δ	boundary layer height at the entry of the domain
α	angle of dihedral plan
ν	kinematic viscosity
u_∞	infinite horizontal velocity
u, v	the two velocity coordinates on (Ax, Ay)
p	pressure
ρ	density

1. Introduction

The dynamics of vorticity creation and transport has been a subject of interest for various internal and external incompressible flows. Different numerical methods such as vortex methods, LES and DNS techniques are used

* Correspondence and reprints.
E-mail address: Iraj.Mortazavi@math.u-bordeaux.fr (I. Mortazavi).

to achieve an accurate estimation of the vorticity behaviour in complex geometries. One of classical benchmark case studies is the flow on a backward facing step. This flow has been analysed for laminar evolution and higher Reynolds numbers. A similar geometry is the flow over a sloping surface. In this case, the reattachment is less sensitive and more progressive, so the vorticity creation and the size change occur in a more progressive way too. It therefore allows one to pursue how the eddy generation changes with the Reynolds number: the dominant rule of boundary layer vorticity then becomes a measure of the wall influence on the flow dynamics. Furthermore, this geometry is a partial representation of an airfoil case study. The vortex roll up over an airfoil needs a deep analysis of instantaneous flow dynamics. To do this analysis, some powerful coherent structure diagnostic tools are necessary.

In this work, three different vortex diagnostic methods are compared to obtain a better understanding of boundary layer influence on the flow dynamics involving a complete analysis of vorticity, the Vorticity Threshold Criterion (VTC), and the Weiss Criterion (WC). These three techniques are compared to find a suitable understanding of all flow characteristics (the swirling dynamics produced downstream of the discontinuity point of the dihedral) for a range of laminar to transitional Reynolds numbers.

The computations on this dihedral plane are performed using a 2D DNS method. The Weiss criterion, arising from the analysis of the incompressible Euler equations ([1] and [2]), is adapted to this case study (compressible viscous flow, with Mach number equal to 0.2). This adaptation is permitted due to low compressibility of the flow (there is no shock). This criterion is consistent with the more classical vorticity threshold criterion, and therefore prooves an appropriate tool to isolate coherent vortices. Once the computational and diagnostics tools steps accomplished, a detailed analysis of the swirling procedure is performed for Reynolds number 242, 400, 565 and 800. Two of these Reynolds number correspond to a laminar regime (242 and 400) and the two others cover almost a transitional flow (565 and 800). The study is based on time-averaged quantities analysis as a function of the Reynolds number. The global enstrophy as well as the number and the size of the vortices display prominently increasing heterostrophic behaviour of the concentrated eddy structures with increasing Reynolds number. We note that the principal categorization that we use to define Coherent Structures (CS) is Heterostrophic and Homostrophic. Heterostrophic structures are fast travelling vortices which transport information across the fluid. Homostrophic dipoles usually collapse into a unique larger vortex. Most of the enstrophy of the flow is concentrated in these coherent structures; between them low intensity vorticity filaments are distorted and advected by the velocity field induced by the vortices.

The study is completed by monitoring history points, phase diagrams and Ψ–ω plots. The discretized $\omega = F(\Psi)$ curve permits us to compare efficiently capabilities of diagnostic approaches of Coherent Stuctures (CS) isolation. Finally, the instantaneous dynamics of the vorticity transport will be visualized using different selected tools discussed in the earlier sections. These visualizations are supported by statistics on CS size and interactions at the four above mentioned Reynolds numbers.

The flow domain is shown in the *figure 1*; the computational domain is plotted in dotted lines.

Otherwise, u, v, p and ρ represent respectively the two velocity coordinates on (Ax, Ay), the pressure and the density.

The characteristic Reynolds number is then defined by:

$$Re_{x_0} = \frac{x_0\, u_\infty}{\nu},$$

or

$$Re_\delta = \frac{\delta u_\infty}{\nu}.$$

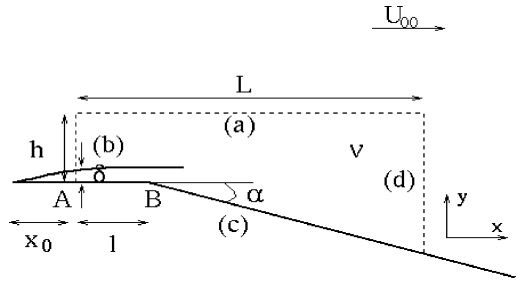

Figure 1. Dihedral configuration.

In this work, x_0 and ν are always constant. Doubling u_∞, Re_{x_0} also is doubled, but Re_δ is multiplied by $\sqrt{2}$ and δ is divided by $\sqrt{2}$. The nondimensional values are:

$$u_{\text{ref}} = u_\infty,$$
$$l_{\text{ref}} = \delta_{200},$$

where δ_{200} is the height of the boundary layer at the entry of the simulation domain for $Re_\delta = 200$. All calculations are performed in this paper using these nondimensional parameters. We choose:

$$L = 48\delta_{200},$$
$$h = 24\delta_{200},$$
$$l = 8\delta_{200}.$$

2. Governing equations and numerical scheme

The governing equations are the 2D compressible Navier–Stokes equations, given in their nondimensionalized formulation by:

$$\frac{\partial U}{\partial t} + \nabla \cdot F(U) = \frac{1}{Re}\nabla \cdot G(U, \nabla U),$$
$$U(t=0) = U_0,$$

with:

$$U = [\rho, \rho u, \rho v, \rho E]^{\mathrm{T}}.$$

The total energy per unit of mass is denoted E, and Re is the numerical Reynolds number. The convective fluxes are given by:

$$F_x(U) = \left[\rho u, \rho u^2 + p, \rho uv, (\rho E + p)u\right]^{\mathrm{T}},$$
$$F_y(U) = \left[\rho v, \rho uv, \rho v^2 + p, (\rho E + p)v\right]^{\mathrm{T}}.$$

The diffusive ones are given by:

$$G_x(U, \nabla U) = [0, \sigma_{xx}, \sigma_{xy}, \beta_x]^{\mathrm{T}},$$
$$G_y(U, \nabla U) = \left[0, \sigma_{xy}, \sigma_{yy}, \beta_y\right]^{\mathrm{T}},$$

with:

$$\beta_x = u\sigma_{xx} + v\sigma_{xy} + \frac{\gamma k}{Pr}\frac{\partial T}{\partial x},$$
$$\beta_y = u\sigma_{xy} + v\sigma_{yy} + \frac{\gamma k}{Pr}\frac{\partial T}{\partial y},$$

where T is the temperature, $\gamma = 1.4$, $k = 1$, $Pr = 0.72$, and:

$$\sigma_{xx} = \frac{4}{3}\frac{\partial u}{\partial x} - \frac{2}{3}\frac{\partial v}{\partial y},$$
$$\sigma_{yy} = \frac{4}{3}\frac{\partial v}{\partial y} - \frac{2}{3}\frac{\partial u}{\partial x},$$
$$\sigma_{xy} = \sigma_{yx} = \frac{\partial u}{\partial y} + \frac{\partial v}{\partial x}.$$

The system is then closed by the state equation:

$$p = (\gamma - 1)\rho T,$$

as well as by the relation:

$$\rho E = \frac{1}{2}\rho\|\boldsymbol{u}\|^2 + \frac{p}{\gamma - 1}.$$

The Navier–Stokes equations are solved using a DNS method based on unstructured triangular grids with 201×101 nodes. To obtain a good resolution of the boundary layer and the separation point instabilities, the grid distribution is refined near the dihedral wall regions in the normal direction to the boundary and horizontally in the vicinity of point B. For the high value of Re_δ ($Re_\delta = 800$) and to obtain a satisfactory solution at low Reynolds numbers, 11 nodes are implemented on the heigth of the boundary layer at the entry of the domain.

The numerical scheme is fully explicit in time. In order to obtain the solution U_l^{n+1} at node A_l and time t^{n+1}, we need to evaluate the global space derivatives of the flux $D(U_l^n)$ at node A_l and time t^n:

$$D(U_l^n) = -\left(\frac{\partial F_x}{\partial x} + \frac{\partial F_y}{\partial y}\right)_l^n + \frac{1}{Re}\left(\frac{\partial G_x}{\partial x} + \frac{\partial G_y}{\partial y}\right)_l^n.$$

The convective derivative $(\frac{\partial F_x}{\partial x} + \frac{\partial F_y}{\partial y})_l^n$ is evaluated by a vertex based finite volume method associated to the Roe solver. In order to obtain the second-order accuracy in space, a M.U.S.C.L. procedure is added to increase the order of the interpolation. No flux limiter is needed, since the solutions considered in this paper don't have any discontinuity. The diffusive derivative $(\frac{\partial G_x}{\partial x} + \frac{\partial G_y}{\partial y})_l^n$ is evaluated by a classical P_1 finite element method. This is a centered process, with the second-order accuracy in space. Finally, the temporal integration of the global space derivatives is performed with a modified Euler scheme (Heun method), with second-order accuracy in time. A mass lumping procedure is applied to make the matrix of the linear system diagonal, and a Courant–Friedrich–Levy condition has to be respected to ensure the numerical stability of the scheme.

As the domain is bounded, it is necessary to specify appropriate boundary conditions. In this work, four boundary conditions are applied.

On the boundary (a) (*figure 1*), the non-reflecting boundary condition with a pressure extrapolation is used. Then, the inviscid boundary conditions are imposed by specifying the component of the vector L composed of

the amplitudes of the characteristic waves normal to this boundary and given by:

$$L = \begin{pmatrix} (u_n - c)\left(\dfrac{\partial p}{\partial n} - \rho c \dfrac{\partial u_n}{\partial n}\right) \\ u_n\left(c^2 \dfrac{\partial \rho}{\partial n} - \dfrac{\partial p}{\partial n}\right) \\ u_n\left(\dfrac{\partial u_\tau}{\partial n}\right) \\ (u_n + c)\left(\dfrac{\partial p}{\partial n} + \rho c \dfrac{\partial u_n}{\partial n}\right) \end{pmatrix} = \begin{pmatrix} L_1 \\ L_2 \\ L_3 \\ L_4 \end{pmatrix}.$$

u_n is the normal velocity to the boundary, and u_τ the tangential one. Since this is a subsonic flow, we have $u_n + c > 0$. Thus, L_4 is evaluated using a discretization inside the computational domain. If $u_n > 0$, L_2 and L_3 are evaluated in the same way, whereas if $u_n \leqslant 0$, then $L_2 = L_3 = 0$. Finally, since $u_n - c < 0$, we use a pressure recall in order to specify the static pressure:

$$L_1 = K(p - p_\infty),$$

where K is a constant. The viscous boundary conditions imposed are:

$$\frac{\partial \sigma_{n\tau}}{\partial n} = 0,$$
$$\frac{\partial^2 T}{\partial n^2} = 0.$$

On the boundary (b), which is a subsonic inflow, the two components of the velocity as well as the temperature are strongly imposed using the Blasius profile:

$$u = u_{\text{imp}}(y),$$
$$v = v_{\text{imp}}(y),$$
$$T = T_0.$$

The density ρ is deduced from the continuity equation, compatible with the previous boundary conditions imposed [3]. The pressure is then obtained using the state equation. No viscous boundary condition is imposed, because of the methodology used in [3].

On the boundary (c), which is an isothermal no slip wall, the velocity is cancelled and the temperature specified as:

$$u = 0,$$
$$v = 0,$$
$$T = T_0.$$

Once there is a time step, the density is deduced from the continuity equation, respecting the previous boundary conditions [3]. The pressure is then obtained using the state equation.

On the boundary (d), Hernandez [4] pointed out that the non-reflecting boundary condition with a pressure recall, similar to the one used for the boundary (a), did not give physical results. To overcome this difficulty,

Bruneau and Creusé proposed a new way to evaluate L_1 when $u_n > 0$ (or L_1, L_2 and L_3 when $u_n < 0$). The idea is to use a reference stationnary flow obtained on the same configuration with a buffer zone at a lower Reynolds number, as well as a reference convection velocity, which is the velocity at infinity, to discretize these L_i values ($i = 1, 2$ or 3) in a more consistant way with the physics of the problem [5]. The vortices are then correctly transported out of the computational domain, with a good damping of reflecting acoustic waves. The viscous boundary conditions imposed are the same as for the boundary (a).

3. Identification of coherent structures

The first step of this work is to define a Coherent Structure (or Concentrated Structure). A defintion is given by Lugt as "many rotating particles turning around a common center" [6]. Jeong and Hussain [7] have generalized the Weiss criterion to three dimensions and have compared the efficiency of different detection techniques. In this work, we compare the complete vorticity field representation to the vortex threshold identification method as well as to Weiss criterion, and we try to find out the best compromise to study and visualize the dynamics of vorticity. The flow is two-dimensional and slightly compressible.

3.1. The vortex threshold criterion

To isolate the eddy structures, one idea should come from focusing in areas with a definite (or higher) value of vorticity:

$$|\omega| = \left| \frac{\partial v}{\partial x} - \frac{\partial u}{\partial y} \right| > \varepsilon, \tag{1}$$

where ε is a parameter depending on the studied flow. This criterion is based on the fact that the intensity of the vorticity inside the eddy structures is higher than in the outside. One possibility to define ε in internal flows is to choose it equivalent to the average enstrophy of the flow [8]. This choice can reflect in a basic way the flow dynamics, but needs a finite bounded domain terminology and should not be used in our case with open boundaries.

3.2. Weiss criterion and variable density problems

Here we consider an inviscid incompressible fluid, with corresponding 2D Euler equations:

$$\begin{aligned} \frac{\partial \boldsymbol{u}}{\partial t} + \boldsymbol{u} \cdot \nabla \boldsymbol{u} &= -\boldsymbol{\nabla} p, \\ \operatorname{div} \boldsymbol{u} &= 0, \end{aligned} \tag{2}$$

where $\boldsymbol{u} = (u, v)$ is the velocity vector and p is the pressure. To study the vorticity field deformations, Weiss proposes to combine the definition of $\nabla - / * \omega$. Taking successively the curl and then the gradient of (2), one obtains:

$$\frac{\mathrm{d}\boldsymbol{\nabla}\,\omega}{\mathrm{d}t} + A^t \cdot \boldsymbol{\nabla}\,\omega = 0,$$

where A is the velocity gradient tensor:

$$A = \begin{pmatrix} \dfrac{\partial u}{\partial x} & \dfrac{\partial u}{\partial y} \\ \dfrac{\partial v}{\partial x} & \dfrac{\partial v}{\partial y} \end{pmatrix}.$$

Considering that this tensor varies slowly compared to the vorticity gradient, this equation can be taken as a linear equation with constant coefficients. Then the behaviour of the vorticity gradient is locally determined by the nature of the eigenvalues of A. These eigenvalues are simply the roots of the following equation:

$$4\lambda^2 = \sigma^2 - \omega^2, \tag{3}$$

where σ corresponds to the deformation:

$$\sigma^2 = \frac{1}{2}\left[4\left(\frac{\partial u}{\partial x}\right)^2 + 4\left(\frac{\partial v}{\partial y}\right)^2 + 2\left(\frac{\partial v}{\partial x} + \frac{\partial u}{\partial y}\right)^2\right].$$

The Weiss criterion is then defined. In the areas where $\sigma^2 - \omega^2$ is positive, the eigenvalues are real and the motion is principally hyperbolic, then the rotation is dominated by the deformation. These areas are not considered as vortical regions. In the areas where $\sigma^2 - \omega^2$ is negative, the eigenvalues are imaginary and the motion is principally elliptic, then the deformation is dominated by the rotation. These regions are considered as vortical regions.

In fact, the condition $\omega^2 > \sigma^2$ may be considered as a 'vorticity threshold criterion', with ε depending essentially on the local deformation.

Let us now justify and validate this method to a weakly compressible flow with a variable ρ. Combining the continuity equation with the compressible Euler equations, we obtain:

$$\frac{\partial \boldsymbol{u}}{\partial t} + \boldsymbol{u} \cdot \nabla \boldsymbol{u} = -\frac{1}{\rho} \nabla p.$$

Then taking the curl and then gradient of this equation, the following relationship is defined:

$$\frac{\mathrm{d} \nabla \omega}{\mathrm{d}t} + A^t \cdot \nabla \omega = -\frac{2}{\rho^3}(\nabla \rho \times \nabla p)_s \nabla \rho + \frac{1}{\rho^2}\nabla(\nabla \rho \times \nabla p)_s, \tag{4}$$

where $(a \times b)_s$ is the unique non-zero component of the vector product of vectors a and b.

Nevertheless, the right term of equation (4) may be neglected for the two following reasons. First, the flow studied in this work is slightly compressible, then the values of $\nabla \rho$ are small. Furthermore, if p could be considered as an unique function of ρ, we would write:

$$p = f(\rho),$$

and:

$$\nabla p = \frac{\partial p}{\partial \rho} \nabla \rho.$$

So, vector products in (4) would be nullified. This numerical hypothesis is verified by observing the time evolution of the density and the pressure on three monitoring points of the flow (*figure 2*), as well as their instantaneous isolines on the whole flow domain (*figure 3*). Both *figures 2* and *3* confirm the similarity of the

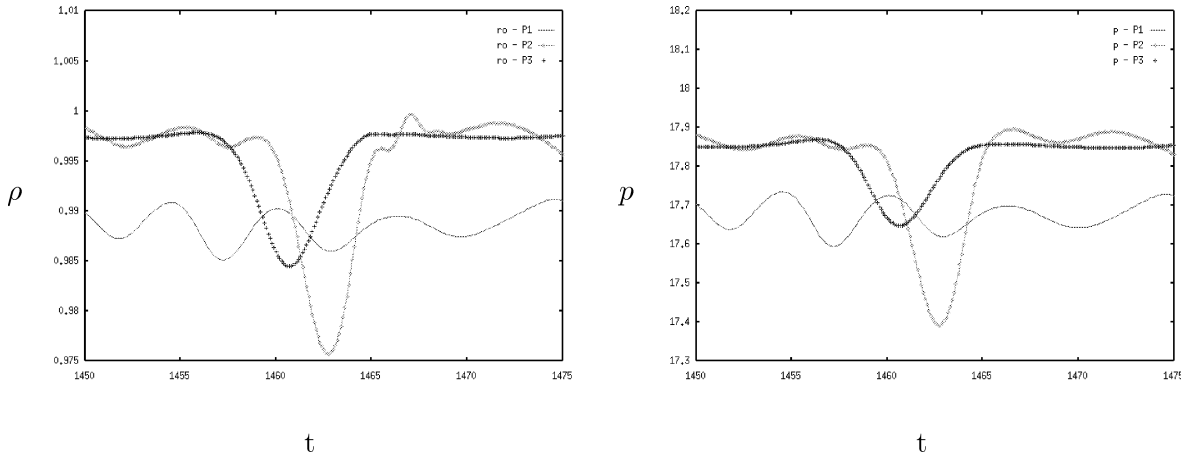

Figure 2. Density and pressure signals at three points in the flow.

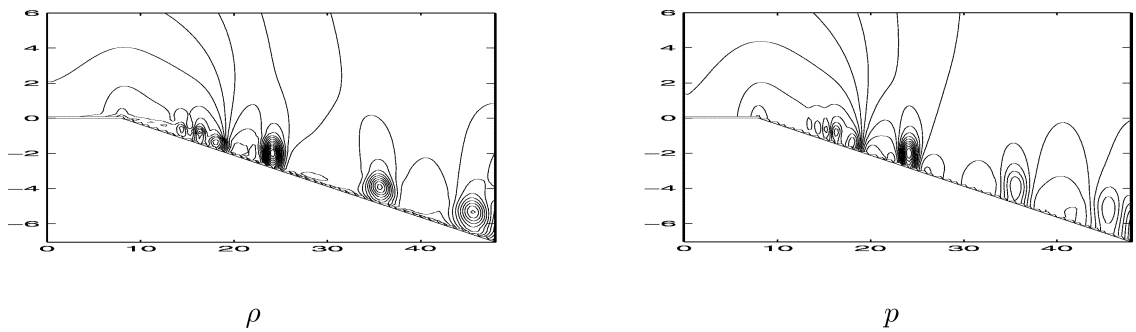

Figure 3. Density and pressure isolines.

ρ and p behaviour either in time and in space. This numerical observation displays a good correlation between the ρ and p values.

Using these considerations, we can justify the validation and application of the Weiss criterion to slightly compressible flows. Now, to have a better idea about the complementarity of these techniques, every criterion is verified for two different flows.

The first case study corresponds to a high Reynolds number incompressible channel flow with obstacles [9] (*figure 4*). This kind of flow is an interesting test problem for our study because of the rich topology of vortex creation and transport. An instantaneous plot of the vorticity field confirms the existence of vortical structures of various size, shape and intensity (*figure 4(a)*). With the Weiss Criterion, these vortices cover almost 81% of the total enstrophy in the flow versus 15% of overall occupied surface (*figure 4(b)*). To compare the two detection techniques we chose first ε_1 in a way to permit to the vortex threshold method to detect 81% of the total enstrophy in the vortical zones (*figure 4(c)*). Then as a second choice, ε_2 is used to permit to the threshold technique to fit the vortical areas with the 15% of total computational domain surface (*figure 4(d)*). Also the VTC has been used, choosing ε^2 equal to the average value of the enstrophy (*figure 4(e)*). Three main observations should be mentioned. The first one is that for the same value of enstrophy in the threshold technique and the Weiss criterion (81%), the detected surface is diminishing from 15% to 7% for the first one. The size of CS is equally decreased and some of them are even disappeared. However, the size of vortices

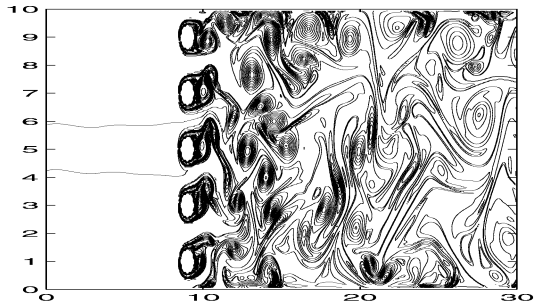

(a) Vorticity isolines

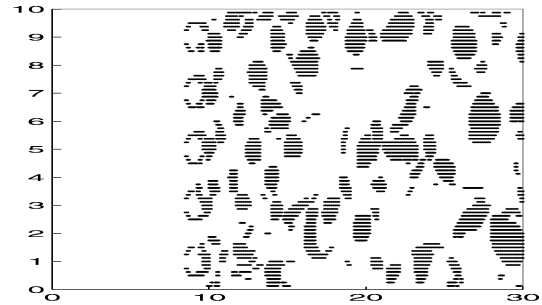

(b) Weiss: 81 % Z, 15 % S

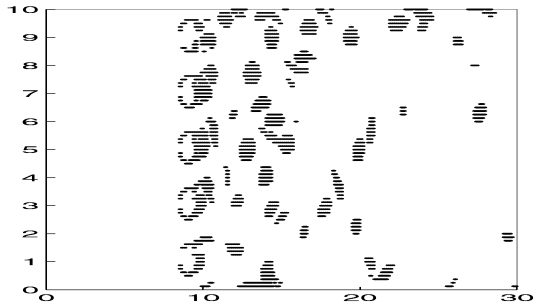

(c) Vorticity threshold: 81 % Z, 7 % S

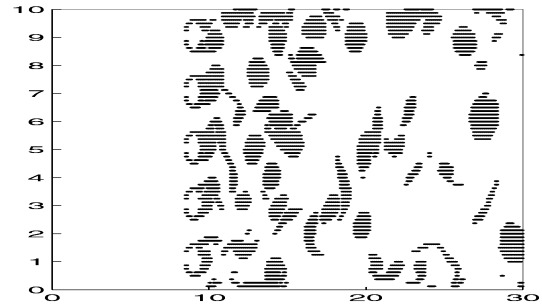

(d) Vorticity threshold: 93 % Z, 15 % S

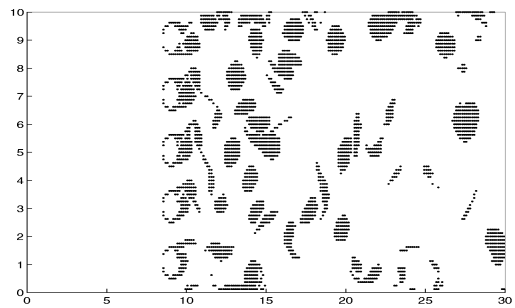

(e) Vorticity criterion for the channel flow, $\varepsilon^2 = \frac{1}{S}\int\int_S \omega^2 \mathrm{d}S$.

Figure 4. Comparison of the different criteria in the channel.

just behind obstacles are slightly increased for the VTC. In the second case we see that by choosing equal vortex occupied surfaces for the two criteria, the VTC shows a higher global enstrophy value (93% compared 81% for Weiss). The size of CS remains almost the same between the two methods, but a few structures seem to be neglected by the threshold technique. Finally, for the choice of ε^2 equivalent to the average value of the enstrophy, we find a closer behaviour between WC and VTC. Nevertheless, the VTC represents the non-coherent vortex formation procedure around the obstacle, still neglecting a few CS. This is not the same for the WC that focuses more on transported eddies.

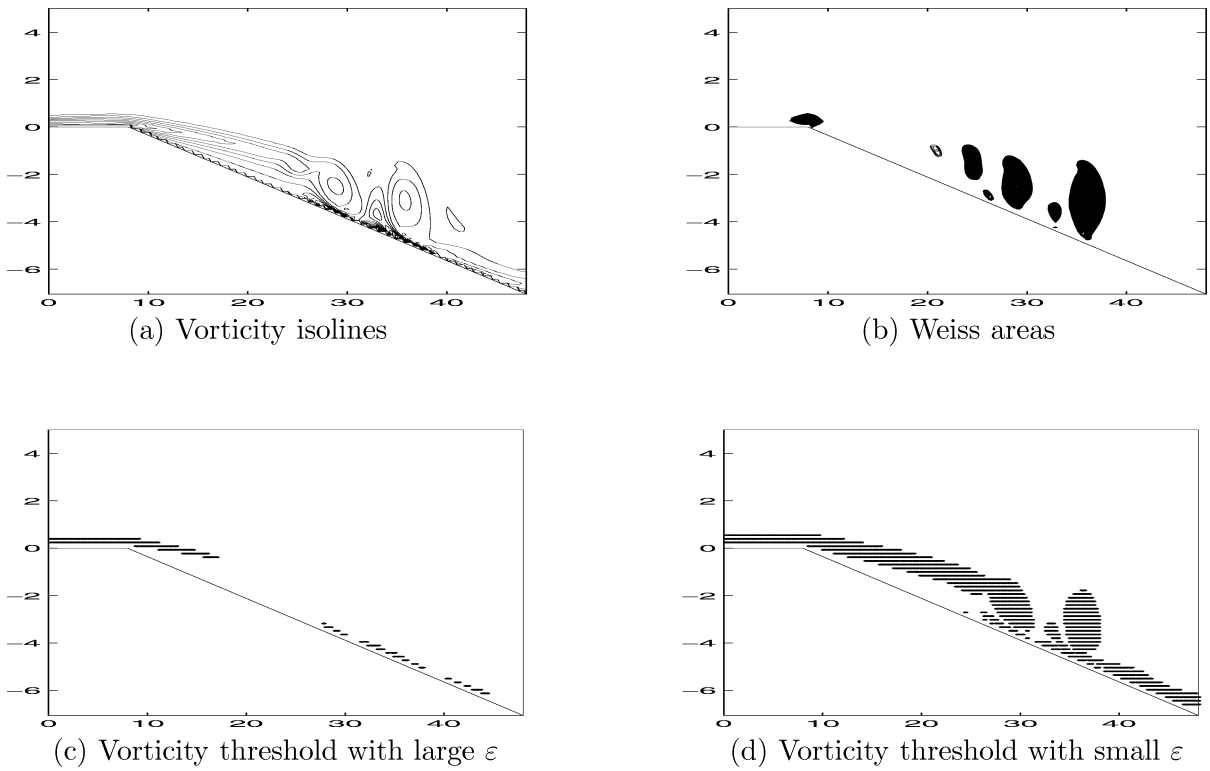

Figure 5. Comparison of the different criteria on the dihedral.

The second flow corresponds to a compressible viscous flow on a dihedral plane with quite low Reynolds numbers ($Re_\delta = 400$). The vorticity field plot confirms the creation of some vortical zones in the downstream of the discontinuity point B (*figure 5(a)*). The vorticity detected by the VTC is observed for two different values of ε, one small and the other one large. For the larger value of ε, the concentrated vortices are merely identified except of the boundary layer vorticity with its high shear properties (and therefore high rotational behaviour) (*figure 5(c)*). For a smaller ε, the structures are present but mainly covered inside the boundary layer extension, and VTC does not isolate them from each other and makes the detection task quite difficult (*figure 5(d)*). However, the WC distinguishes and separates several CS in the dihedral slopping transport domain (*figure 5(b)*).

Obviously, one should ask: why not use the vorticity isolines directly (the vorticity field)? To answer to this question, it should be mentioned that the vorticity field is a natural and important source of information on the rotational flow dynamics. Nevertheless, sometimes we need to isolate coherent structures and to determine not only their size and their number in the flow, but also their individual characteristics such as enstrophy, circulation etc. For these studies, the vortex detection criteria like WC (and its extensions [2,10]) offer more efficient tools. They permit detection of CS in a wide range of individual enstrophy values (small or large even in the boundary layers) and the definition of their size independantly from any cutoff (ε) that is quite difficult to define in flows like the second case study (because of the arbitrary choice of the computational domain). Therefore, the WC (and its extensions) are recommanded to identify CS. It should be noted that the WC and the VTC are highly complementary. The VTC compares the vorticity to an experimentally chosen value. Such as the average enstrophy intensity for flows within a bounded domain. However this ‘cutoff’ value is globally defined in the flow domain. The global choice is arbitrary when compared to high vorticity domains. A global

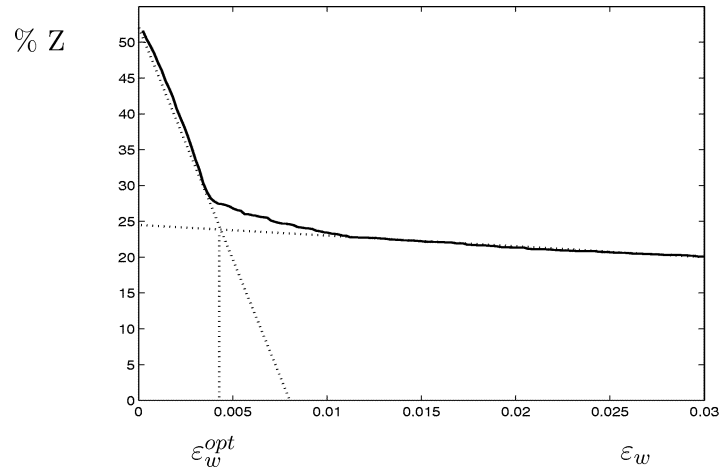

Figure 6. The ε_{opt} determination.

cutoff of the form ($|\omega| > \varepsilon$) means that $|\omega|$ varies linearly versus ε (or ω^2 versus ε^2), and is not adjusted to local non-linearities and variations. But the extended WC locally determines domains where ω^2 dominates σ^2 ($\omega^2 > \sigma^2$). The new cutoff respects local physical properties of the flow related to the choice of separate CS.

However, numerically it's necessary to determine a 'tolerance gap', to improve the verification:

$$\omega^2 - \sigma^2 > \varepsilon_w,$$

where ε_w is a small positive value, that should be chosen asymptotically. Let us consider either a laminar Poiseuille flow, or a laminar boundary layer over a flat plate. These flows which can be considered as the 'background' flow of the previous test cases, have a value of $\omega^2 - \sigma^2$ which is roughly zero. However, a small peturbation can push $\omega^2 - \sigma^2$ to a locally positive value mimicking a vortical behaviour with no real vortex structure presence. For the dihedral geometry, the proportion of the CS enstrophy (using WC) to the global flow is plotted versus the parameter ε_w (*figure 6*). As the figure shows, two different behaviours are distinguished at the right and the left hand side of $\varepsilon_w^{opt} = 0,004$, defined as the cross-section of tangents to the curve at 0 and infinity. For $0 < \varepsilon_w < \varepsilon_w^{opt}$, the high variation of the enstrophy value corresponds to shear zones of the boundary layer that can be identified by the WC only if ε_w is very small (when ω^2 is very close to σ^2). These zones disappear when ε_w is increasing, even very slightly. For $\varepsilon_w > \varepsilon_w^{opt}$, an asymptotically state is acheived. That means: when ε is increasing, the regions identified by the WC stay almost unchanged. They correspond therefore, to the definition of CS. In these regions, ω^2 is sensibly higher than σ^2. To verify these conditions, many numerical experiments have been performed for a wide range of ε_w values. They fulfilled entirely the above mentioned remarks concerning the choice of ε_w^{opt}. This value of ε_w^{opt} is large enough to remove the background flow, and small enough to distinguish the ensemble of Vortical structures.

Let us now perform an objective locally metastable state test. In two dimensions a coherent vortex can be unambiguously characterized by a functional relation between the vorticity ω and the streamfunction Ψ in the form $\omega = F(\Psi)$, where F is called the coherence function [11]. This relationship has been already used to study the coherency of vortex structures (e.g. [11–13]). It should be mentioned that, the $\omega = F(\Psi)$ relation is basicly devoted to the inviscid and steady flows. Nevertheless, in the case of vortical structures, the inviscid aspect dominates the vortex behaviour. Furthermore, these coherent structures are transported during a long time interval (convection dominated transport), that gives a quasi-steady characteristic to their motion in the special frame associated to each of them. In the present study this technique (in a discrete form) has

been applied in order to investigate the coherent structures observed by different techniques in the flow over a dihedral plane and for two Reynolds numbers: $Re_\delta = 400$ and $Re_\delta = 800$ (*figure 7*). To avoid the noisy effect of the vortex shedding and formation – that apppear as vertical $\Psi = 0$ points – the scattered plots are performed in a domain downstream of the separation point B ($x \geqslant 25$). The first plot (*figure 7(a)*) covers correlation points corresponding to the total flow at $Re_\delta = 400$. This plot generates points that come from all rotational zones (boundary layer and coherent structures) and the background flow. As shown on the plot of the vortex threshold method (*figure 7(b)*), this criterion identifies the rotational zones (coherent or not) directly depending on its threshold parameter. Evidently, this cutoff eliminates a part of the vortical data very abruptly. Finally, the last plot gives a view of correlations ($\omega = F(\Psi)$) for the Coherent Structures identified by the generalised Weiss Criterion (*figure 7(c)*). As shown in the plot, all non-coherent zones (rotationnal or background) are principally vanished. The linear behaviour of this correlation study represents the mainstream of the few CS moving in the flow. The plots (*figure 7(d), (e), (f)*) corresponding to $Re_\delta = 800$, incorporate the increase of the vortical behaviour in all plots. Particularly, in the plot corresponding to the WC, a more concentrated and restricted (but less intense) correlation of linear zones referring to CS is evident. Here, smaller structures are mainly formed at the vicinity of the separation point B. Then, a rise of the number of points on the vertical line is fitted to a decrease of size and intensity of the horizontal line. This behaviour seems to be due to the formation of some intermittent dipolar eddies [14]. The vorticity produced in the boundary layer between the dipole and the no-slip boundary is predominantly accumulated in the wake of the dipole. These scattered plots show again the exclusive focus of the WC on the coherent structures compared to other techniques. Finally, because the original functional frame is fitted and the structures are moving, plots are slightly shifted. Nevertheless, $\omega = F(\Psi)$ criterion is used here, to compare the three extraction criteria and therefore the effect of 'scattering' is the same for the three cases, permitting to have an accurate comparative study.

4. Post-processing and numerical results

4.1. Averaged scalar values

The computational domain to study the vortex dynamics is defined by the region $\overline{D}$ as follows:

$$\overline{D} = \{(x, y) \in D;\, 10\delta_{200} \leqslant x \leqslant 47\delta_{200}\}.$$

Such a domain avoids the zone in the vicinity of the discontinuous point B, where the flow map is very complex. For a computed flow, the parameters are defined by the global enstrophy and the global kinetic energy:

$$Z = \iint_{\overline{D}} |\omega|^2 \,\mathrm{d}\Omega; \qquad E = \frac{1}{2} \iint_{\overline{D}} \rho(u^2 + v^2) \,\mathrm{d}\Omega.$$

Furthermore, defining the function:

$$1^w(x, y) = \begin{cases} 1 & \text{if the Weiss Criterion is verified,} \\ 0 & \text{if not,} \end{cases}$$

it is possible to define the surface, enstrophy, and energy of CS:

$$S^w = \iint_{\overline{D}} 1^w(x, y) \,\mathrm{d}\Omega,$$
$$Z^w = \iint_{\overline{D}} |\omega|^2 1^w(x, y) \,\mathrm{d}\Omega,$$

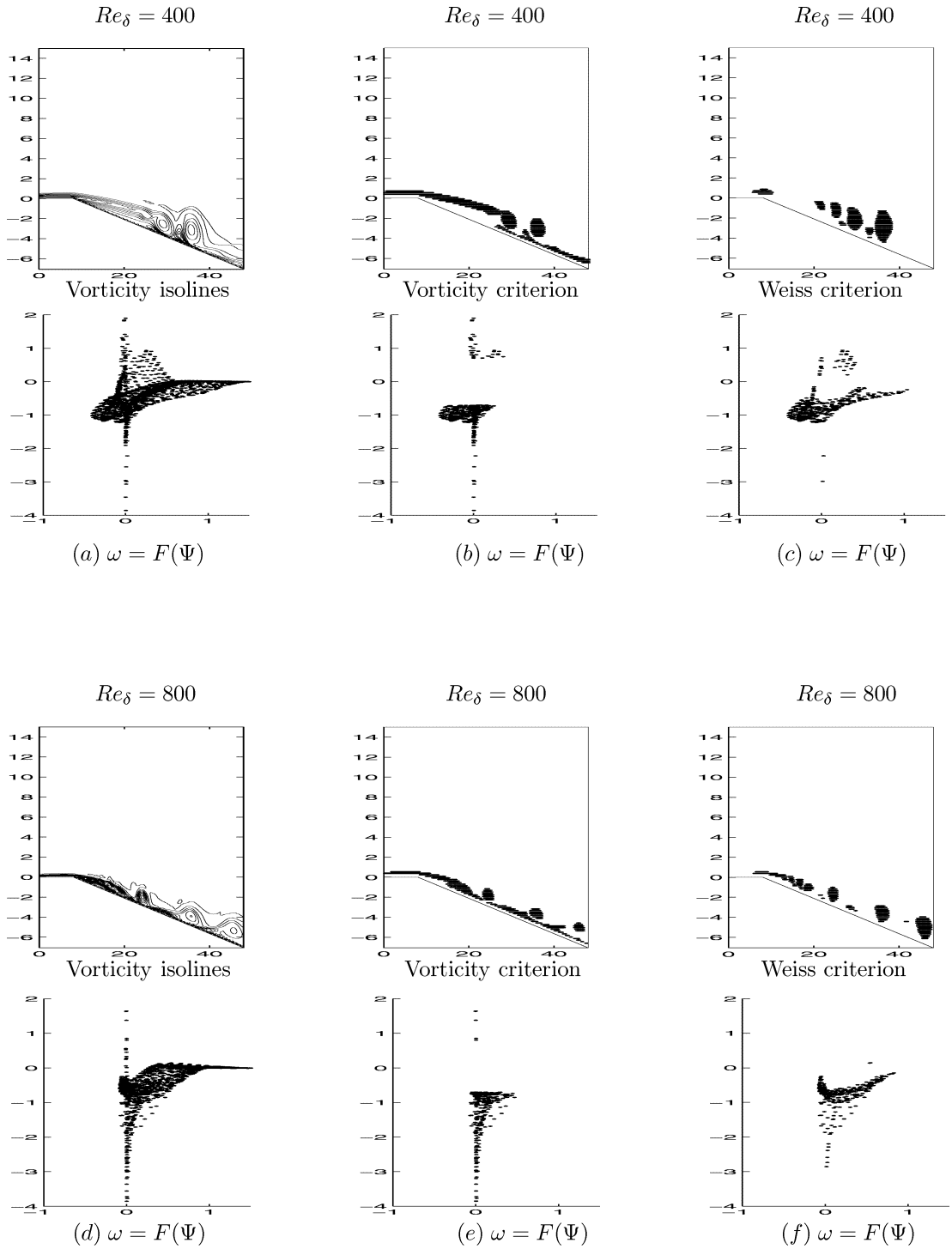

Figure 7. Correlation points.

$$E^w = \frac{1}{2}\iint_{\overline{D}} \rho\left(u^2 + v^2\right) 1^w(x, y)\, \mathrm{d}\Omega.$$

Then we define r_S, r_Z and r_E respectively by the surface ratio, the enstrophy ratio and the kinetic energy ratio. Furthermore, r_Z^c and r_E^c are respectively the concentration coefficients of enstrophy and kinetic energy:

$$r_S = \frac{S^w}{A_{\overline{D}}}; \qquad r_Z = \frac{Z^w}{Z}; \qquad r_E = \frac{E^w}{E};$$
$$r_Z^c = \frac{r_Z}{r_S}; \qquad r_E^c = \frac{r_E}{r_S}.$$

r_S is the proportion of the surface occupied by CS compared to the domain surface $\overline{D}$. In the same way, the proportion of the structures enstrophy or kinetic energy to the global value of the same quantities in the computational domain $\overline{D}$ are given by r_Z or r_E. r_Z^c gives a measure of the 'enstrophy concentration' inside the vortices compared to the overall flow. A constant value of r_Z^c should mean the conservation of the vortical enstrophy concentration in the flow. So for example, if this value is doubled it would mean that either the same surface ratio and the vortical enstrophy concentration is doubled, or for the same vortical enstrophy concentration the surface of the CS is doubled. Similarly, r_E^c represents the 'kinetic energy concentration' inside the CS.

Now, every variable for each vortex can be defined separately. A vortex is characterised as a convex zone inside $\overline{D}$ where the WC of the CS is verified. Its center is defined as the barycentre of its surface and its radius is the radius of a disk with the same surface.

Simulations for different Reynolds numbers are analysed between $t = t_i$ and $t = t_i + 500$. t_i is the initial time of the established regime, and the simulations roughly over 11 fundamental cycles of the flow dynamics. The averaging is performed over this time gap.

Figure 8 shows the sharp increase of the global enstrophy with the Reynolds number (that is directly related to the increase of the rotational behaviour of the flow). The results are not the same for the global kinetic energy which stays constant with the evolution of Re_δ. This is mainly due to the fact that the kinetic energy is an integral value of the velocity and the velocity is present everywhere in the flow (rotationnal or not). This property does not correspond to the enstrophy that is an integral value of the vorticity so directly sensitive to the rotational properties. The relative surface occupied by CS (r_S) diminishes after $Re_\delta = 400$, which relates to the beginning of transition and creation of smaller heterostrophic structures. It should also be mentioned that the increase of r_Z is larger than the decrease of r_S, as shown by the plot of the enstrophy concentration r_Z^c. The direct conclusion of this observation is the increasing concentration of the enstrophy (or the vorticity) in the CS with the Reynolds number. This procedure is combined with the decrease of the boundary layer thickness. Finally, the average number of isolated vortices nv increases with Re_δ and their average radius r_{cs} decreases. *Table I* categorises CS into three different classes of size (value of r_{cs}), confirms this observation. This table shows that the number of small vortices increase with the increase of the Reynolds number. These smaller vortices are fast travelling structures that contribute to the transport of information in the flow. Their increase also means the decrease of larger vortices (large structures disappear completely at $Re_\delta = 800$). Using this table, if we take $r_{\max}$ as the biggest distance between the shape contour of a vortex and its center, the coefficient $\mathrm{def} = r_{\max}/r_{cs}$ should be used to evaluate the average deformation of a CS. Then, $\mathrm{def} = 1$ should correspond to the limit case of a circular vortex. Computations indicate a 20% increase of this parameter when we move from $Re_\delta = 242$ to $Re_\delta = 800$, confirming stronger vortex interactions for increasing Reynolds numbers.

This analysis indicates that for low Reynolds numbers (laminar flow), the CS generate large homostrophic structures [2]. For higher values of Reynolds numbers (transitory), the number of CS increases, their size

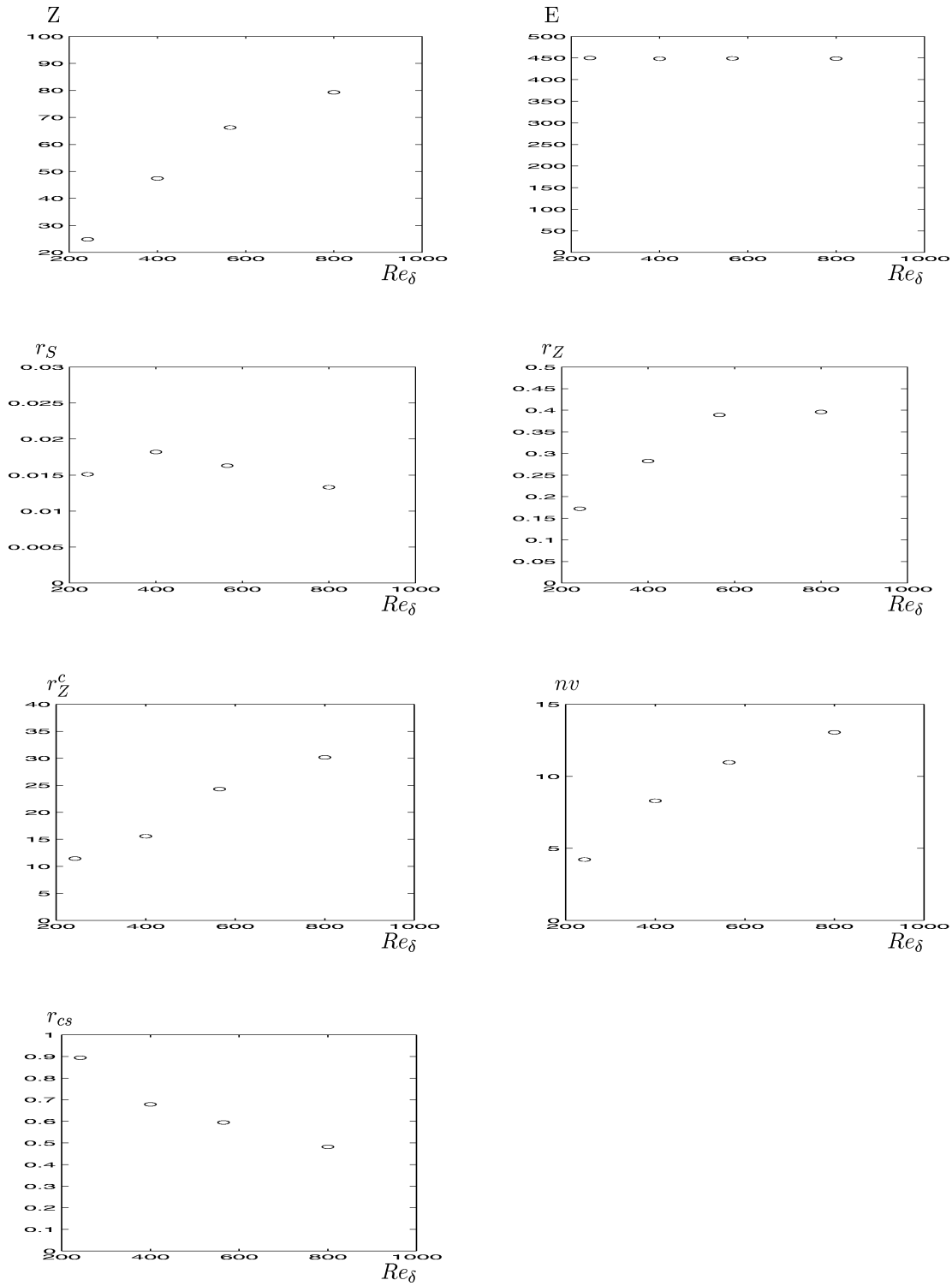

Figure 8. Averaged scalar parameters as a function of Re_δ.

Table I. Classification of CS in function of their radii.

	Small vortices $0 < r_{cs} < 0.66$	Averaged vortices $0.66 < r_{cs} < 1.33$	Large vortices $1.33 < r_{cs}$
$Re_\delta = 242$	46%	20%	34%
$Re_\delta = 400$	57%	26%	17%
$Re_\delta = 565$	59%	38%	3%
$Re_\delta = 800$	75%	24%	1%

becomes smaller, they spin around each other and we observe the onset of some merging processes that is almost a heterostrophic-homostrophic transition behaviour.

4.2. The signal at three monitoring points

Up to now, we have essentially studied the global properties of the flow, using scalar parameters averaged in time. In this section, some local and/or instantaneous properties of the flow will be studied. Three monitoring points are chosen for this study, and their evolution is observed. These points should be chosen appropriately as a function of the importance of the flow events. To choose them appropriately, we plot here the average streamlines for the studied Reynolds numbers. They permit us to better visualize the main recirculation zones and consequently to choose appropriate points.

For every Re_δ, we compute the stream function Ψ, using u and v values and solving the Poisson equation:

$$\begin{cases} -\Delta\Psi = \omega, \\ \qquad + \text{ suitable boundary conditions.} \end{cases}$$

Indeed, the continuity equation can be written:

$$\nabla \cdot \boldsymbol{u} = -\frac{1}{\rho}\frac{\partial \rho}{\partial t} - \boldsymbol{u} \cdot \frac{\boldsymbol{\nabla}\rho}{\rho}.$$

When the Mach number M is small, the relative variation of the density is of the order of M^2. Then, for our configuration $M = 0.2$, and the quantities $\partial\rho/\partial t$ and $\overrightarrow{\nabla}\rho/\rho$ can be neglected in a first approximation. We can then consider that $\nabla \cdot \boldsymbol{u} \approx 0$, letting us compute the stream function Ψ (Poincaré lemma). The velocity vector is defined as:

$$\vec{u} = [u, v] = \left[\frac{\partial\Psi}{\partial y}, -\frac{\partial\Psi}{\partial x}\right] + \overrightarrow{u_P}.$$

In the above relations $\overrightarrow{u_P} = \overrightarrow{\nabla\Phi}$ (where Φ is a scalar velocity potential) represents a potential field corresponding to the fact that the Laplace operator is inverted in a non-unique way [15]. The field $\overrightarrow{u_P}$ is usually related to the presence of rigid boundaries and/or free stream at infinity, hence it will be left out from the present considerations. Then, the above equation can be simplified as:

$$u = \frac{\partial\Psi}{\partial y},$$
$$v = -\frac{\partial\Psi}{\partial x}.$$

We take the following boundary conditions for Ψ:

- *isothermal no slip wall*
  $u = v = 0$, that means $\Psi =$ constant. We then impose on the wall: $\Psi = 0$.
- *Entry flow*
  Considering the boundary layer type velocity profile in the entry, the following approximation seems plausible:

$$u = f(x_0, y) = f(y),$$
$$v \approx 0.$$

  Then, we deduce:

$$\Psi(y) = \Psi(0) + \int_0^y f(y)\,\mathrm{d}y,$$

  that simply means:

$$\Psi(y) = \int_0^y f(y)\,\mathrm{d}y.$$

  So, the stream function value on the entry boundary should numerically obtained by:

$$\Psi(y + \mathrm{d}y) = \Psi(y) + \mathrm{d}y\, f(y).$$

- *Upper boundary*
  For the upper boundary, we consider the semi-infinite boundary conditions, that physically mean:

$$u \approx u_\infty,$$
$$v \approx 0.$$

  This implies $\Psi = g(y)$ or $\Psi =$ constant for a level of this boundary, where the constant value is computed on the upper boundary of the flow entry.
- *Exit flow*
  For this boundary, the previous approximations are no more valid. If we take $\boldsymbol{n}$ as the expanding direction, that is horizontal at the upper point of the exit grid and parallel to the dihedral surface at the downer mesh point, it enables us to progressively localize mesh points on the exit boundary. Then, a Neumann type boundary condition is set as follows:

$$\frac{\partial \Psi}{\partial n} = \nabla \Psi \cdot \boldsymbol{n} = -v \cdot n_x + u \cdot n_y,$$

  and is applied as the exit boundary condition in this paper.

The time averages streamlines ($\overline{\Psi}$) show that with the increase of Re_δ, the average recirculation zone becomes smaller and moves towards the discontinuity point B (*figure 9*). This behaviour is similar to the flow past a backward-facing step. If the Reynolds number continues to increase, the recirculation zone approaches more and more the discontinuity point. This mechanism means a progressive motion of the CS formation zone towards point B and an increase of the instabilities in the transitional regime. As mentioned previously, the monitoring points used in this article are chosen with respect to the average streamline plots. The point P_1 is located at the centre of the average recirculation zone of the flow at $Re_\delta = 800$. In the same way, the points P_2 and P_3 are chosen at the centre of the recirculation zones of $Re_\delta = 565$ and $Re_\delta = 400$ flows.

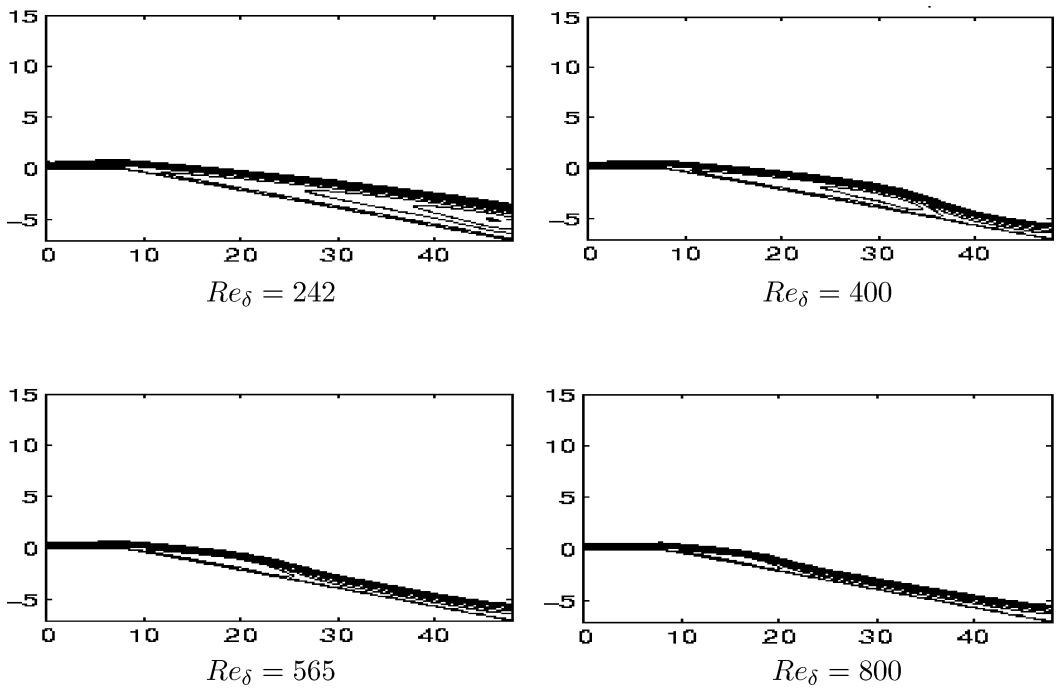

Figure 9. Time averaged streamlines.

The phase diagrams $v = f(u)$ are plotted in the *figure 10* for each Reynolds number. The first remark about this figure is that for all Reynolds numbers the amplitude is very low on the upstream of average recirculation zones. This amplitude has a rapid increase moving downstream of these regions, diminishing in the upstream of the flow. This result confirms that the upstream region corresponds to the formation areas of CS and is mainly diffusion dominated [16]. The center of the average recirculation zone is located approximately on the vortex shedding areas, imposing a radical increase of the phase diagram. These regions are connected to the CS transport zones (convection dominated) until the exit, that correspond to a slight decrease of this amplitude. *Figure 11* is devoted to the time evolution study of the velocity modulus $\|\overrightarrow{u}(t)\|$ for every monitoring point. As the figure shows, upstream of the recirculation zones, no characteristic velocity oscillation occurs. The most complex oscillations and therefore the most complex frequency variations occur in the neighbourhood of the center of the recircualtion zones which are related to the vortex shedding procedure. Afterwards, the interaction and merging of CS progressively generate larger structures with lower transport frequencies.

4.3. Flow visualization for $Re_\delta = 400$ and $Re_\delta = 800$

This section is devoted to visualising the isolines of Ψ, ω, $1^w(x, y)$ and p, on a fundamental period of the flow which is $T_{400} = 45$ for $Re_\delta = 400$, and $T_{800} = 25$ for $Re_\delta = 800$. This visualization study permits us to observe either the eddy formation and shedding procedure or the vorticity transport and interaction events. One of these two cases is laminar and the other transitional, providing a good comparison for our observations.

Figures 12 and *13* confirm the previous results that the shedding region is located in the neighbourhood of the centre of the average recirulation zones. Furthermore, Weiss regions are obviously detected after the shedding has occured and correspond naturally to the transport of the CS in the flow. A comparison of CS detected by

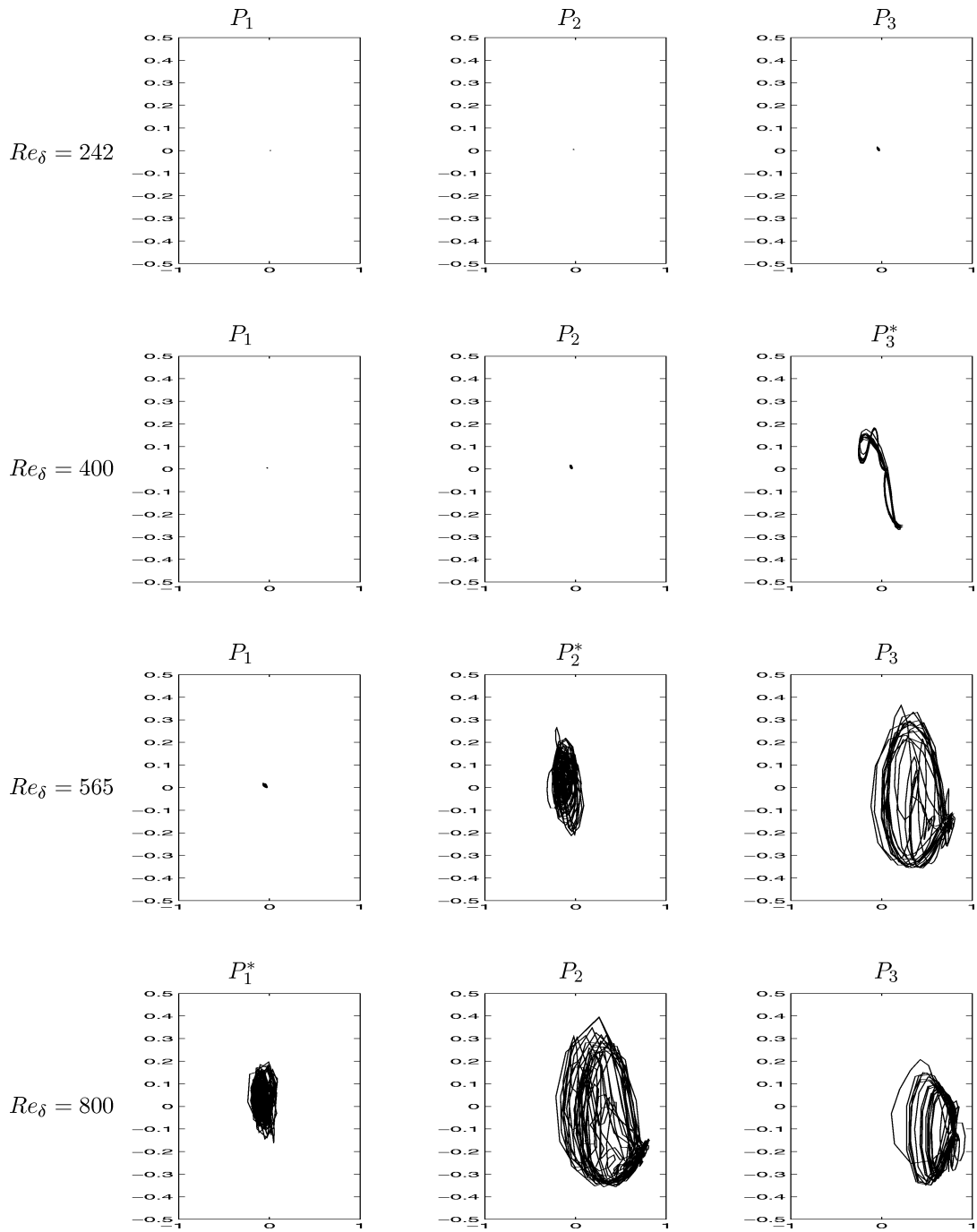

Figure 10. Phase plane $v = f(u)$. P_i^* is the center of the averaged recirculation area at the considered Re_δ.

the WC and the corresponding vorticity field, pressure field and streamlines confirm the good capability of the WC to isolate the CS from not only the background flow but also other non-coherent rotational regions.

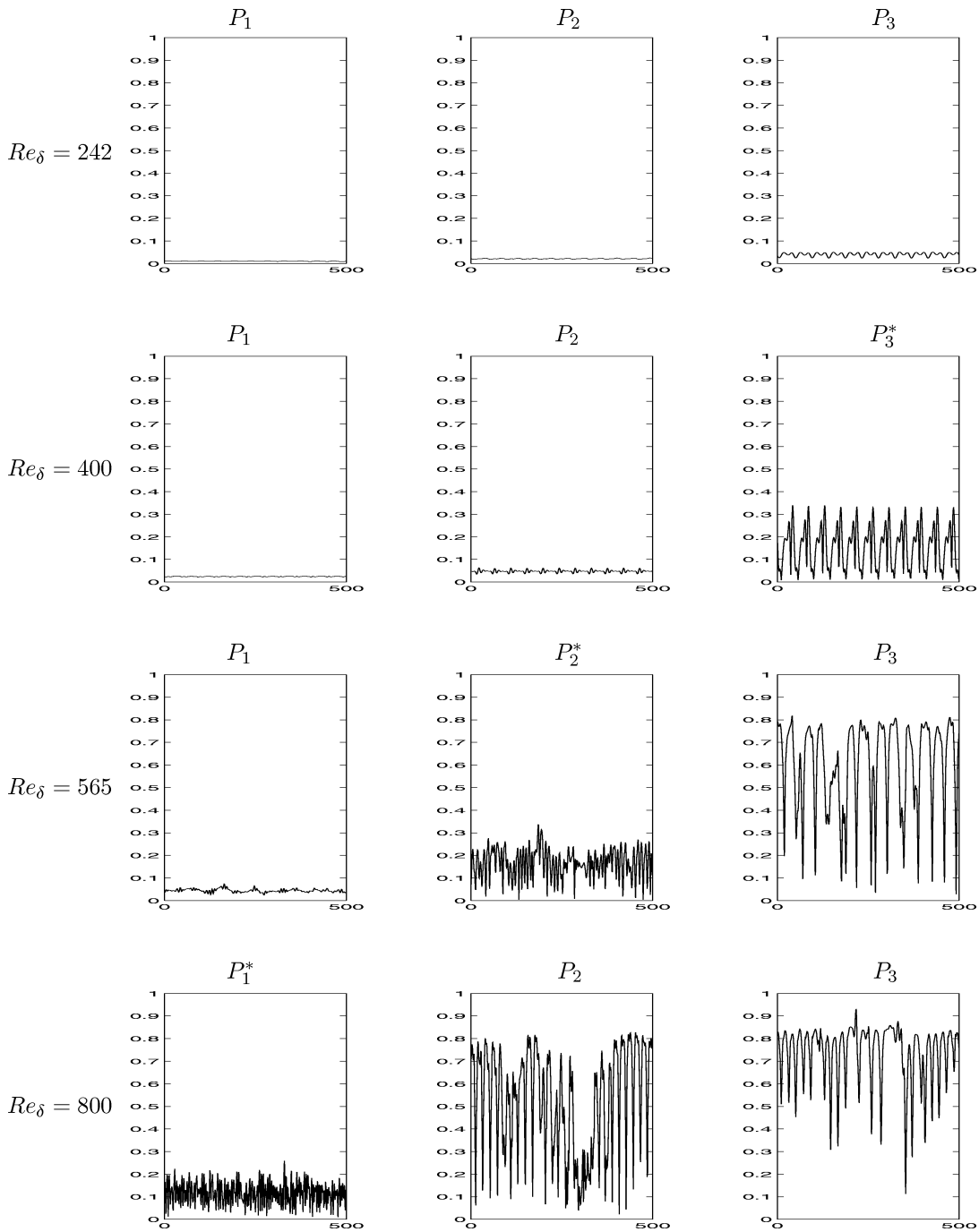

Figure 11. $\|\boldsymbol{u}(t)\|$. P_i^* is the center of the averaged recirculation area at the considered Re_δ.

Finally, a comparison between the flow at Reynolds 400 and 800 shows that the CS are shed in the flow closer to the discontinuity point with the increase of the Reynolds number. This observation is consistent with the higher frequency of the vortex creation at higher Reynolds numbers, that is equally accompanied by a

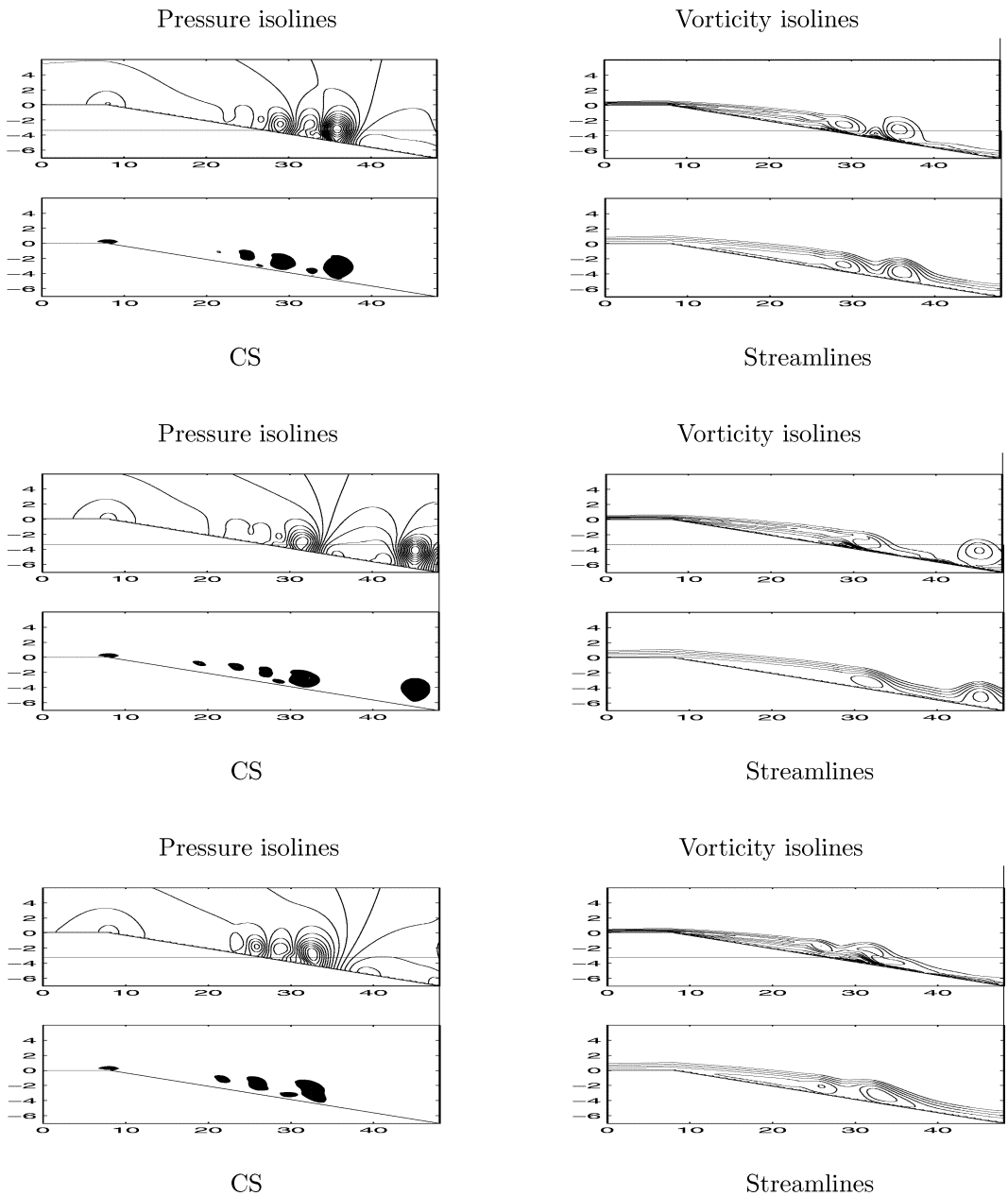

Figure 12. $Re_\delta = 400$: $t = T_{400}$ (top), $t = T_{400} + 2T_{400}/5$ (middle), $t = T_{400} + 4T_{400}/5$ (bottom).

decrease of their size. These smaller structures are injected and transported more rapidly than in the case of lower Reynolds numbers (see also [16]). This property means an increase of the number of heterostrphic structures (that transport information across the fluid) for relatively higher Reynolds numbers ($Re_\delta = 800$ here). This increase is also accompanied by a higher rate of collapsing and merging, generating heterostrophic-homostrophic transition between CS in the flow map. These results are completely according to the statistics presented in the *table I*. Inversely, for $Re_\delta = 400$ the progressive formation of large slow-moving homostrophic structures (with less coherent and more dissipative properties) almost characterize the flow behaviour.

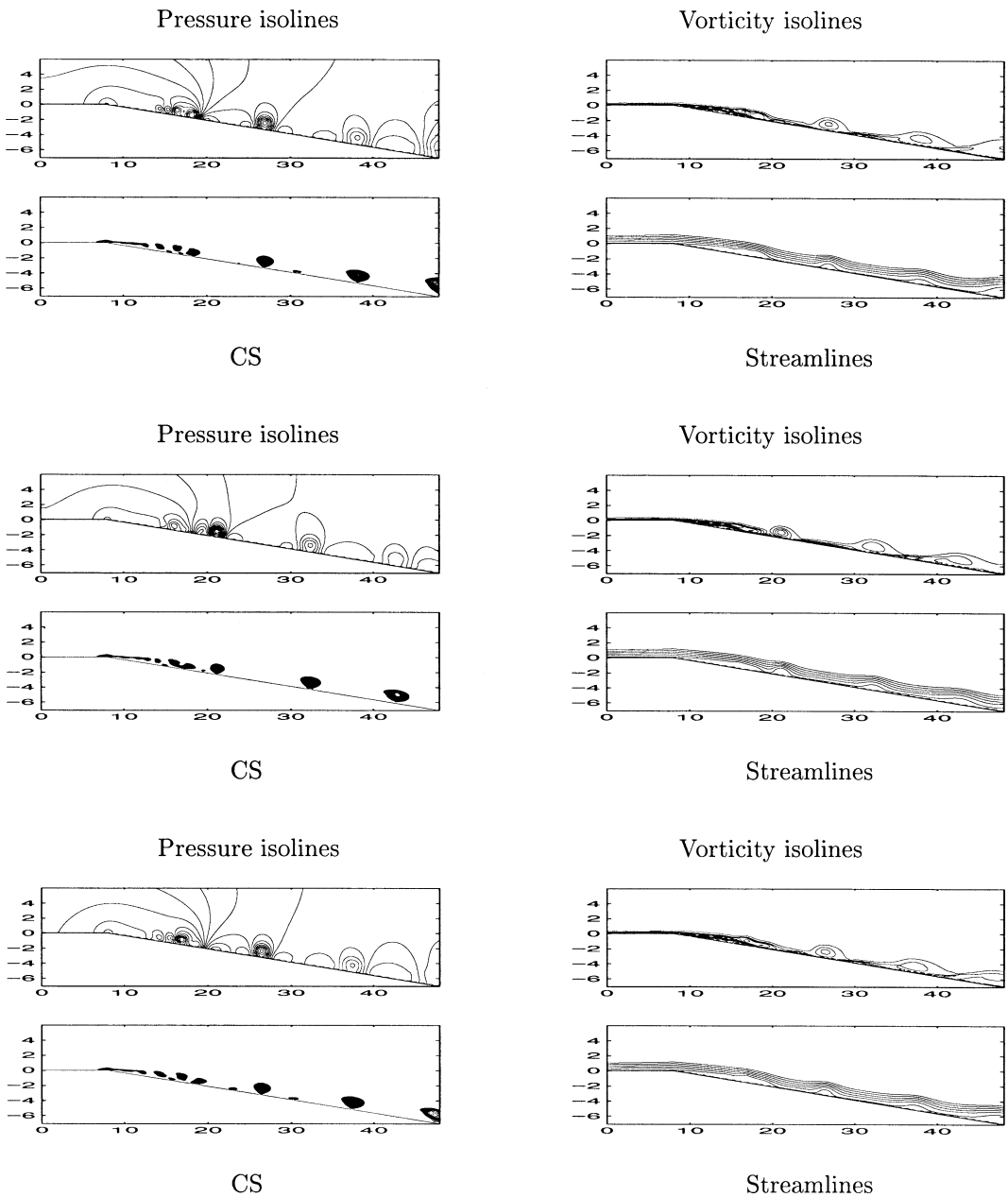

Figure 13. $Re_\delta = 800$: $t = T_{800}$ (top), $t = T_{800} + 2T_{800}/5$ (middle), $t = T_{800} + 4T_{800}/5$ (bottom).

5. Conclusion

This work was devoted to studying the vortex dynamics of compressible laminar and transitional flows on a dihedral plane. The work was based on four different Reynolds numbers: two laminar (225 and 400), and two transitional (565 and 800). At the beginning we analysed different Coherent Structure detection methods (Weiss Criterion and Vorticity Threshold Criterion). We generalised the WC for low Mach number compressible flows and demonstrated its capability to be applied to these kind of flows. Then, we compared two criteria to the

general vorticity field representation and showed that, if in internal flows with a suitable choice of the threshold cutoff (average enstrophy ε^2) two criteria give similar results, in arbitrary domains the WC present a better and more natural alternative to capture CS (extracting not only the background flow but also other non-coherent rotational zones). Then, we presented a methodology to choose an 'optimal tolerance gap' which permits one to smooth approximately coherent zones. This smoothing value was chosen when the global enstrophy evolution curve began to achieve a plateau. The last objective of this section was to study CS using Ψ–ω plots. We determined that the WC permits us to extra ct the 'only-CS' regions capturing principally points corresponding to them. Also, this curve enabled us to observe the transitional behaviour at $Re_\delta = 800$, with a higher rate of vortex roll-up in the boundary layer and the replacement of the CS shedding area toward the discontinuity point B (shorter horizontal point area and more points on the vertical line).

Another section of the paper was devoted to studying the CS evolution for a wide range of Reynolds numbers using some averaged scalar values like enstrophy and kinetic energy. A sharp increase of the CS vorticity concentration with the Reynolds number was observed. However, the enstrophy concentration for the transitional regime had an approximately constant evolution. This property seems to be due to the creation of smaller eddies that also contain lower scalar values. This analysis indicates that for low Reynolds numbers (laminar flow), the CS create large structures called homostrophic. For higher values of Reynolds numbers (transitory), the number of CS increases, their size becomes smaller, they spin around each other and we observe the onset of some merging processes that is almost a heterostrophic-homostrophic transition behaviour. To complete this study, monitoring point analysis (phase diagram and velocity modulus time evolution) was accomplished on three important points of the flow domain (again for the range of Reynolds numbers from laminar to transitory). These plots confirmed that: (a) the shedding area moves up with the Reynolds number; (b) the transitory oscillations arise in the shedding sections (these sections are mainly diffusion-dominated [16]), which correspond mainly to the core of the average recirculation zones; (c) the remaining of the flow domain is transport (convection) dominated with more regular dipolar structures interactions. Finally, a dynamic visualization of the flow events confirmed these observations, offering a better view of the strong dynamics of the vorticity formation and transport, generated by complex mixing, merging, shedding and roll-up procedures.

This study should be a cornerstone for another step that will be devoted to the active control of the boundary layer over a dihedral plane, that should drastically modify the behaviour of the vortex wall interactions.

Acknowledgments

The authors wish to thank Marie Farge, Kai Schneider, Spencer Sherwin and the reviewers for helpful comments and suggestions. They are also grateful for the support they received from the "groupe de travail mécanique des fluides active" of Dassault-CMLA (ENS Cachan).

References

[1] Weiss J., The dynamics of enstrophy transfer in two-dimensional hydrodynamics, Physica D 48 (1991) 273–294.
[2] Basdevant C., Philipovitch T., On the "Weiss criterion" in two-dimensional turbulence, Physica D 73 (1994) 17–30.
[3] Poinsot T.J., Lele S.K., Boundary conditions for direct simulations of compressible viscous flows, J. Comput. Phys. 101 (1992) 104–129.
[4] Hernandez G., Contrôle actif des instabilités hydrodynamiques des écoulements subsoniques compressibles, Thèse Cerfacs, 1996.
[5] Bruneau C.H., Creuse E., Towards a transparent boundary conditions for the compressible Navier–Stokes equations, Int. J. Numer. Meth. Fl. 36 (2001) 807–840.
[6] Lugt H.G., The dilemma of defining a vortex, in: Muller U., Roesner K.G., Schmidt B. (Eds.), Recent Developments in Theoritical and Experimental Fluid Mechanics, Springer, 1979, pp. 309–321.
[7] Jeong J., Hussain F., On the identification of a vortex, J. Fluid Mech. 285 (1995) 69–94.
[8] Babiano A., Basdevant C., Legras B., Sadourny R., Vorticity and passive scalar dynamics in 2d turbulence, J. Fluid Mech. 183 (1987) 379–398.

[9] Bruneau C.H., Greffier O., Kellay H., A numerical study of grid turbulence in two dimensions, in: Bruneau C.H. (Ed.), Sixteenth International Conference on Numerical Methods in Fluid Dynamics, Lecture Notes in Physics, 1998, pp. 129–134.
[10] Herbert V., Larcheveque M., Staquet C., Identification of organized structures in two-dimensional turbulence, C. R. Acad. Sci., to appear.
[11] Farge M., Schneider K., Kevlahan N., Non-Gaussianity and coherent vortex simulation for two-dimensional turbulence using an adaptative orthogonal wavelet basis, Phys. Fluids 11 (8) (1999) 2187–2201.
[12] Verzicco R., Flor J.B., van Heijst G.J.F., Orlandi P., Numerical and experimental study of the interaction between a vortex dipole and a circular cylinder, Exp. Fluids 18 (1995) 153–163.
[13] Flor J.B., van Heijst G.J.F., Stable and unstable monopolar vortices in a stratified fluid, J. Fluid Mech. 311 (1996) 257–287.
[14] Clercx H.J.H., Maassen S.R., van Heijst G.J.F., Decaying two-dimensional turbulence in square containers with no-slip or stress-free boundaries, Phys. Fluids 11 (3) (1999) 611–626.
[15] Protas B., Analysis and control of aerodynamic forces in the plane flow past a moving obstacle – Application of the vortex method, PhD thesis, université Paris 6, 2000.
[16] Mortazavi I., Giovannini A., Dyagnostics of the vorticity formation and transport in bluff-body flows using a hybrid vortex-finite element method, Int. J. Fluid Dynam., to appear.